Bidirectional reflectance measurement of tungsten samples to assess reflection model in WEST tokamak ⊘

M. Ben Yaala ✉; M.-H. Aumeunier; R. Steiner; ... et. al

Check for updates

CrossMark

View Online

Export Citation

Articles You May Be Interested In

Application of UB matrix formalism in inelastic neutron scattering experiments at BATAN's SN1/TAS

AIP Conference Proceedings (November 2021)

Substrate impact on the low-temperature growth of GaN thin films by plasma-assisted atomic layer deposition

Journal of Vacuum Science & Technology A (June 2016)

Dynamic bidirectional reflectance distribution functions: Measurement and representation

Journal of Laser Applications (January 2008)

AIP Publishing

Bidirectional reflectance measurement of tungsten samples to assess reflection model in WEST tokamak

View Online   Export Citation   CrossMark

M. Ben Yaala,[1,2,a] M.-H. Aumeunier,[3] R. Steiner,[1] M. Schönenberger,[4] C. Martin,[5] M. Le Bohec,[3] C. Talatizi,[3] L. Marot,[1] and E. Meyer[1]

AFFILIATIONS

[1] Department of Physics, University of Basel, Klingelbergstrasse 82, CH-4056 Basel, Switzerland
[2] Department of Biomedical Engineering, University of Strathclyde, Glasgow G1 1QE, United Kingdom
[3] CEA, IRFM, F-13108 Saint-Paul-Lez-Durance, France
[4] Nano Imaging Lab, Swiss Nanoscience Institute, University of Basel, Klingelbergstrasse 82, 4056 Basel, Switzerland
[5] School of Theoretical and Applied Science, Ramapo College of New Jersey, Mahwah, New Jersey 07430, USA

[a] Author to whom correspondence should be addressed: marwa.ben-yaala@strath.ac.uk

ABSTRACT

This paper presents the measurement of the bidirectional reflectance distribution function of tungsten (W) samples and the resulting reflection models in the nuclear fusion device WEST (tokamak). For this, an experimental gonio-spectrophotometer was developed to fully characterize the material's optical and thermal-radiative properties of metallic samples with different roughnesses. Ray-tracing photonic simulation was then carried out to predict the photon behavior in a fully metallic environment as a function of reflectance measurement. Low emissivity (0.1 at 4 μm) and highly specular reflectance (fitting with a Gaussian distribution around the specular direction with a small width lower than 10°) are found for W samples. These measurements have been used as input for the photonic simulation, and the resulting synthetic image reproduced the reflection features well on the upper divertor, detected in WEST infrared experimental images.

Published under an exclusive license by AIP Publishing. https://doi.org/10.1063/5.0046140

I. INTRODUCTION

Infrared (IR) thermography is a reliable and robust method widely used in fusion reactors to monitor and protect the plasma-facing components (PFCs) by measuring their surface temperature in real-time. Unlike carbon walls previously used in fusion devices, the future fusion reactor, also called tokamaks, will be fully metallic.

In particular, ITER fusion tokamak PFCs are made of beryllium and tungsten, which makes the analysis of the infrared (IR) thermography measurement more complicated. Indeed, due to their low and variable emissivity (ranging from 0.1 to 0.5), the contribution of the reflected flux in the total collected photon flux by the IR camera will not be negligible anymore and could even be dominant.[1–4] It was reported that the contribution of the reflected flux from the upper port visible/infrared system of the ITER can

lead to overestimation of the surface temperature of up to 20% for the hottest targets and up to 90% for the coldest surfaces.[1] These false hotspots resulting from the incorrect interpretation of the IR measurements could lead to excessive interruptions of the plasma shots as well as to limitations on scenario development toward high performance.

Photonic simulation capable of accurately predicting the contribution of reflected flux within the collected flux by the camera has also been developed in order to be able to discriminate the parasitic light reflections to other thermal events.[5–7] This has shown that the finest knowledge of optical and thermal-radiative properties of materials is essential to understand and predict the photon behavior in a fully reflective and radiative environment well.

This paper presents an experimental setup developed to fully characterize the bidirectional reflectance distribution function (BRDF) of material samples. Directional and total emissivities

are also deduced by indirect measurements. The results are presented for tungsten samples at different roughnesses. Tungsten is the material chosen as the most critical component in the tokamak (divertor) and which is exposed to the highest heat loads and for which the roughness can be changed during the experimental campaign (erosion/deposition phenomena). The relation between reflectance/emittance and roughness is also discussed in this paper. Experimental results are then used as input for the photonic simulation, and the resulting IR synthetic image is compared with the experimental image of the WEST tokamak.

II. RAY-TRACING PHOTONIC SIMULATION

The photonic simulation code is based on Monte Carlo ray-tracing (SPEOS CAA V5 based software from ANSYS-SPEOS[8]) capable of propagating the ray through the complex geometry of the tokamak and takes the multiple inter-reflections of the ray in the vacuum vessel into account.

As output, the simulation delivers two images: the "real" image that reproduces the IR camera view and includes the reflected flux from the metallic walls and the "reflection-free" image resulting from material emission only. The reflection-free image is, therefore,

used to quantify the contribution of the reflected light from PFCs and evaluate the real surface temperature. To do so, the simulation is based on three input models: namely, the thermal scene model, the camera and optic model, and the photon–material interaction model. While the thermal model presents the 3D distribution of the heat flux on PFCs and their resulting surface temperature, the optical model includes the camera geometrical parameters [the field-of-view (FOV), image size in the focal plane, and wavelength range] to reproduce the camera view. The accuracy of simulated results will depend on the accuracy of each model used as input for the ray-tracing code. The study in this paper aims to improve the model of photon–material interaction from experimental measurements of a particular optical material property known as the bidirectional reflectance distribution function.

III. SURFACE REFLECTANCE MODEL

The reflected light behavior is described with a combination of three main components shown in Fig. 1: Lambertian, specular, and Gaussian reflectance—the so-called glossy reflection. Lambertian reflection occurs with an equal spread of reflecting light in all directions from a surface. Specular reflection occurs with directional
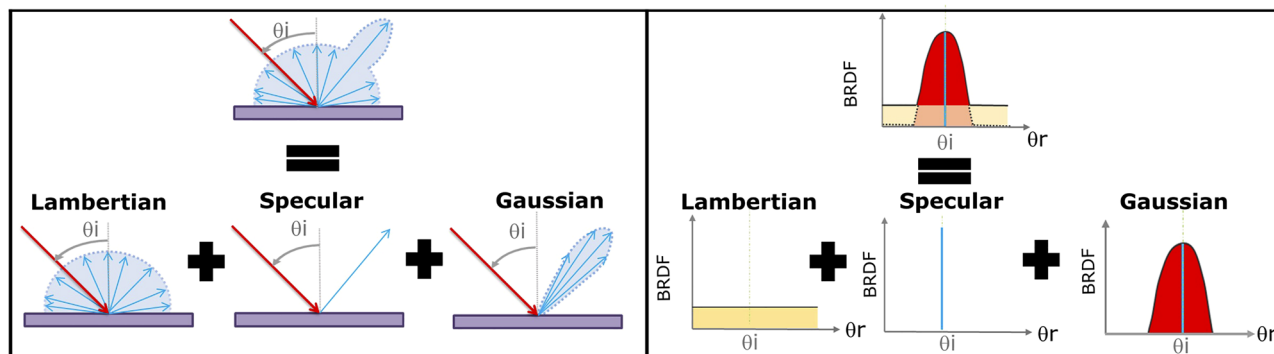

FIG. 1. Illustration of the reflectivity model as a combination of Lambertian, specular, and Gaussian components: (left) beam geometry and (right) the BRDF of each component.
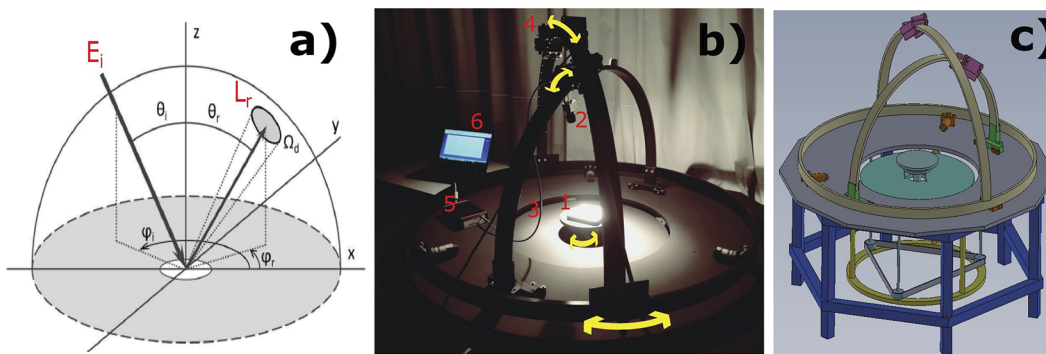

FIG. 2. (a) BRDF parameters and (b) and (c) the overview of the BULGO gonioreflectometer: the (1) sample holder, (2) collimator, (3) optical fiber, (4) light source, (5) spectrophotometer, and (6) LabVIEW computer software.

reflection of light from the surface, with the incident angle equal to the reflection angle defined by Snell–Descartes laws. In practice, most of the specular material's reflection is a combination of a pure major directional specular component with a diffuse component following a Gaussian model, for which the reflected light has a Gaussian probability of being reflected with a particular angle around the main direction.

Reflection models are described through a BRDF that relates the energy arriving at a surface from the direction of illumination to the reflected intensity in the direction of the detector,

$$BRDF(\lambda, \theta_i, \phi_i, \theta_r, \phi_r) = \frac{dL_r(\lambda, \theta_r, \phi_r)}{dE_i(\lambda, \theta_i, \phi_i)}, \quad (1)$$

where λ is the wavelength of the incident light, E_i is the incident spectral irradiance, L_r is the reflection spectral radiance, (θ_i, ϕ_i) is the direction of the incident light, and (θ_r, ϕ_r) is the direction of the reflected light, as presented in Fig. 2(a).

In order to collect BRDF experimental data, a specialized measurement device called the gonioreflectometer is used. The full description of this device and the measuring procedure are described in Sec. IV.

IV. EXPERIMENTAL SECTION

A. BULGO spectrophotometer

1. Setup description

The Basel University Laboratory GOniospectrophotometer (BULGO) is a device with four degrees of rotational freedom designed to measure the optical properties of materials by measuring the directional reflectance of the sample as a function of angles of illumination and observation. The incident light on a material surface comes from the light source aperture. The light viewed by the detector is delimited by its aperture. Both the direction of illumination (θ_i, ϕ_i) and viewing direction (θ_r, ϕ_r), in spherical coordinates, can vary independently within the hemisphere above the material sample. An overview of this gonioreflectometer is shown in Figs. 2(b) and 2(c). The instrument consists of

(i)   a rotatable and height adjustable sample holder,
(ii) a vertical half-circular arc supporting the zenith motion of the light source
(iii) a horizontal circular rail for the azimuthal motion of the light source, and
(iv) a vertical stationary half-circular arc to support the zenith motion of the light collimator.

The light source mounted on the apparatus is a tungsten halogen 50 W Ushio lamp inside a Lowel assembly of 12.7 cm diameter. The assembly allows two possible settings of the lamp, which are "spot" and "flood." The spot position is used for yielding a more parallel light beam, increasing the homogeneity of the illuminated area over oblique illumination angles. In both configurations, the light coming from the lamp is not collimated, which implies that it reaches the surface of the sample with different angles. In order to correct the reflected flux from non-parallel rays, a pure specular aluminum reference sample was measured. Its BRDF represents

the angular distribution of the light source, and it is, therefore, deconvoluted from the BRDF of measured samples to get corrected results describing the pure reflectance of the sample surface. The lamp, which produces 1250 lumen, covers the electromagnetic spectrum in the region of 0.35–2.5 μm and provides a sufficiently strong signal for the detector. The detector is composed of a light collimator connected to a spectrophotometer through an optical fiber. The spectrophotometer is an Avantes spectrophotometer (AvaSpec-2048) that measures in the wavelength range from 0.2 to 1.1 μm. The motion and positioning of the BULGO components, as well as the operation of the spectrometer, are remotely controlled by the Lab-VIEW program. The system is, therefore, able to operate in a fully automatized mode.

2. Alignment process and assembly precision

For BRDF measurement, the sample reflected flux collected by the spectrophotometer is compared to the reference reflectivity (Spectralon, polytetrafluoroethylene). The Spectralon exhibits the highest diffuse reflectance of any known material or coating over the UV-VIS-NIR (near infrared) region of the spectrum. Its deviation from the pure Lambertian reflectance was measured by its manufacturer/supplier, and this deviation was translated into a correction factor that is considered in the calculation of the BRDF.

Section IV A 2 describes the alignment process and its accuracy. The sample holder was adjusted in the horizontal plane in order to align the sample surface with the detector and the light horizontal planes. The sample was then placed in the center of the sample holder, and its height was adjusted to the same height of the Spectralon reference in order to measure under the same geometrical configurations.

Focusing of the setup was performed by focusing the detected signal in the optical fiber. This was carried out by using a laser connected to the end of the optical fiber (instead of the spectrophotometer). The collimator lens position was then varied until reaching the position where the beam footprint is not dependent on the object distance. Due to the reversibility of the optical path, this step permits finding the collimator focal length to get a focused beam inside the optical fiber.

The geometric accuracy of the sensor FOV was tested by placing a sharp thin stick in the collimator position. This was accomplished by moving the stick over the zenith arc that supports the detection system while tracing the maximal deviations of the stick from the center of the sample holder on graphic millimeter paper. The observed deviations among the six zenith positions (0° to 75°) were smaller than 1.2 cm in both x and y directions. The same procedure was followed for the zenithal and azimuthal rotation of the light source, and a maximum deviation of 0.8 cm was found in both cases.

In order to determine the position of the measurement spot on the sample while the detector is rotating on the zenith arc, the deviation of the collimator FOV across the target was examined by connecting a laser to the end of the optical fiber. The footprint was recorded on millimeter paper for each zenith position of the detector. At zero incidence, the laser footprint on the sample was circular with a 1 cm diameter (corresponding to the collimator diameter) that became distinctively elliptical toward higher zenith angles, reaching around 3.9 cm at 75°. This limits the smallest size of

samples that can be measured with the BULGO to 4 cm with the condition of surface homogeneity over the detection area. The impact of detector footprint variation on the BRDF measurement is canceled by measuring the reference Spectralon and the sample with the same geometrical configurations.

3. Measurements

A 2-h warm-up period was maintained for both the spectrophotometer and the light source before starting any measurement. The warming-up of the spectrophotometer is essential to stabilize dark current while the warming-up of the light source is used to provide a stable and homogeneous intensity distribution over time.

Any sequence of positions can be programmed and executed from the LabVIEW program, and the spectrophotometer detects the reflected intensity from the target surface. The full measurement cycle starts with the measurement of a Spectralon reference followed by a dark current measurement of the spectrophotometer (by closing the collimator aperture), and finally, a measurement of the sample under the same geometrical configurations as those used for the Spectralon is carried out. As also described by Murray-Colman and Smith,[9] the sample BRDF is then calculated as follows:

$$BRDF = C_f \times \frac{\frac{I_{sample}}{T_{sample}} - \frac{I_{dark}}{T_{dark}}}{\frac{I_{Spectralon}}{T_{Spectralon}} - \frac{I_{dark}}{T_{dark}}}, \quad (2)$$

where I is the intensity of reflected light detected by the spectrophotometer, T is the integration time automatically adjusted by the program to have enough measured intensity, and C_f is the reflectance of the Spectralon.

4. Validation

Due to the complexity of the BRDF measurement process and the multiplicity of parameters that can influence the precision of the measurement (stability of the light source, stability of the spectrophotometer and its dark measurement, angular positioning on four axes, etc.), the measurement error cannot be calculated precisely. However, another way to estimate this error is by measuring a specific sample with another goniospectrophotometer and comparing the results to BULGO measurements. For that, an Inconel tile sample from the JET tokamak[10] was measured and compared to the results obtained with the Field Goniometer System (FIGOS) at the University of Zürich, Switzerland.[11]

The measurement position sequence was the following: The sample holder was fixed at 0°, the light position was at 10° and 0° in the zenith and azimuth directions, respectively, and the spectrometer was moved on its zenith supporting arc by a step of 15°. BRDF results obtained for both systems are shown in Fig. 3. Both devices deliver very similar BRDF values for the same sample, with a 2.1% maximum difference between both measurements confirming the accuracy of the BULGO system.

B. Further characterization techniques

Using the BULGO, the bidirectional reflectance of a surface cannot be measured for some angular combinations of the light
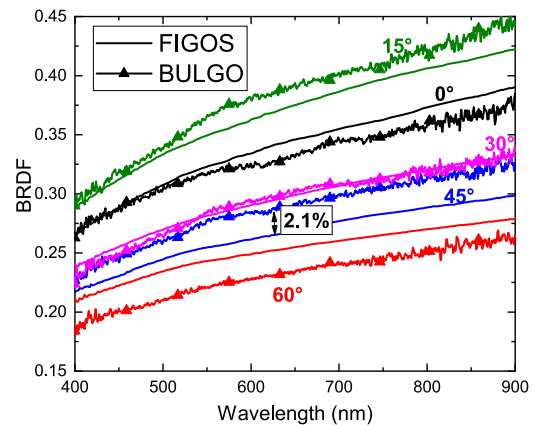

FIG. 3. BRDF of the JET Inconel tile measured by BULGO and FIGOS goniophotometers.

source and detector. In particular, the 0° light source zenith position over the 0° sensor position is a "blocked" angular combination due to the shadow casting effect on the sample. This artifact is attributed to the sensor being directly underneath the light source. Furthermore, the high grazing angle (in the range of 80° to 90°) cannot be measured due to mechanical restrictions. Different methods are thus required to extrapolate the full BRDF at these extreme geometrical configurations.

The 0° incidence normal reflectance was measured using a UV-vis-near infrared (NIR) spectrophotometer Varian Cary 5 equipped with a 110 mm diameter integrating sphere under nearly normal incidence (3°20') in the wavelength range of 0.25–2.5 μm.[12] An integrating sphere is designed to collect the reflected radiation (diffuse or total) from a sample. It consists of a spherical cavity with a polytetrafluoroethylene coating of high diffuse reflectance on its inner wall. The sample reflects the incident light, which is repeatedly reflected by the spherical cavity's inner wall. This produces diffuse light, which enters the detector. The measurement with this spectrophotometer does not allow measuring the pure specular reflectivity part due to the sphere aperture, which includes the reflected flux around the specular direction (±1°6).

To measure the pure specular reflectivity, a third setup is used consisting of a spectral ellipsometer (Sentech SE 850). This measures the ellipsometric parameters (Ψ and Δ) in the range of 0.3–2.3 μm for angles of incidence of 45°, 55°, and 65°. Δ is the phase difference induced by the reflection, and Ψ is the amplitude component (tan Ψ is the amplitude ratio upon reflection). The fit of these six datasets (fitting routine SpectraRay) using a fixed refractive index and absorption model was performed to obtain the optical constants (refractive index n and extinction coefficient k) of the surface as a function of the wavelength. The pure specular reflectivity of the surface at normal incidence was then recalculated using these optical constants.[12]

The specular reflectance of samples was also measured using a commercial Bruker Vertex 70 Fourier Transform IR (FTIR), with extended spectral ranges, from 100 cm^{-1} (100 μm) to 20 000 cm^{-1} (0.5 μm). The far and mid-infrared measurements were performed

using a combination of broadband beam splitter, high power IR source (globar lamp), and deuterated-triglycine sulfate detector, while for near-IR and visible, a combination of a quartz beam splitter, a high power tungsten lamp, and a silicon diode detector was used. A specular reflection/transmission stage (A510/Q-T) with a fixed angle of incidence of $11°$ was used in conjunction with the FTIR spectrometer. The beam size was between 1 and 1.5 mm, focused close to the center of the sample.

To explore how the roughness of the sample affects the measured BRDF, the surface roughness of the samples was also measured using a three-dimensional laser scanning confocal microscope (3D LSCM, VK-X1100, Keyence). An objective lens of 20 times magnification was used to reconstruct the surface topography. The arithmetical mean height of the surface is calculated over an area of $531 \times 708 \ \mu m^2$.

V. RESULTS AND DISCUSSION

A. BRDF results for W samples with different surface topographies

The plasma-facing components are subjected to high heat flux and other erosion-deposition phenomena, causing a change in the materials' surface state (oxidation) and roughness. This paper focuses on the impact of roughness on the BRDF. To investigate the effect of surface roughness on the BRDF, 4 W samples M100-M103 (shown in Fig. 4) were prepared by mechanical polishing to achieve several roughnesses. The results of their measured average roughness Ra are displayed in Fig. 4.

The total and the diffuse reflectivity were measured in the range 0.25–2.5 μm. This allows us to plot the specular reflectivity in the inset of Fig. 5 (dotted line) on the right side. On that same figure, the
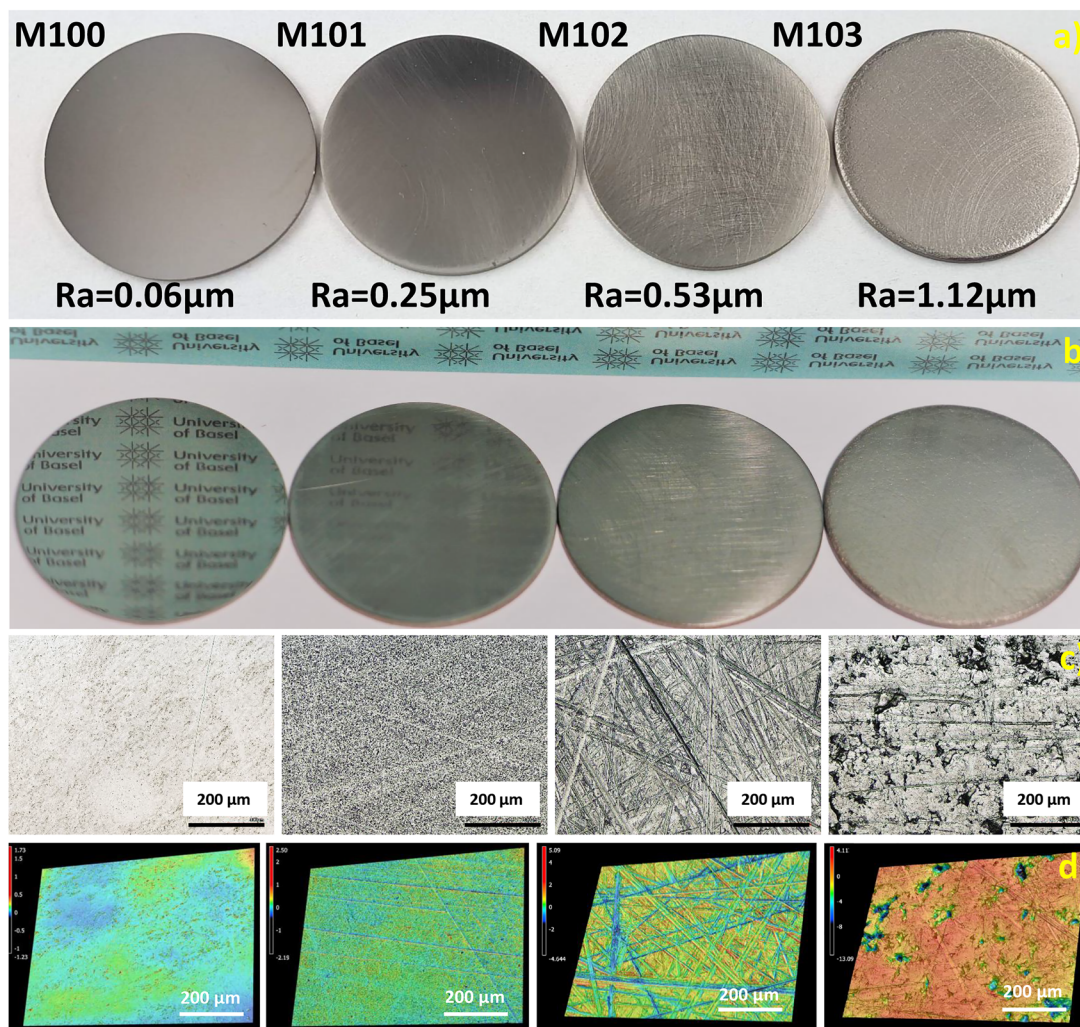

FIG. 4. (a) W samples mechanically polished to different roughnesses, (b) a picture to show their mirror reflections, and (c) and (d) their corresponding surface topography measured by Laser Scanning Confocal Microscopy (LSCM).
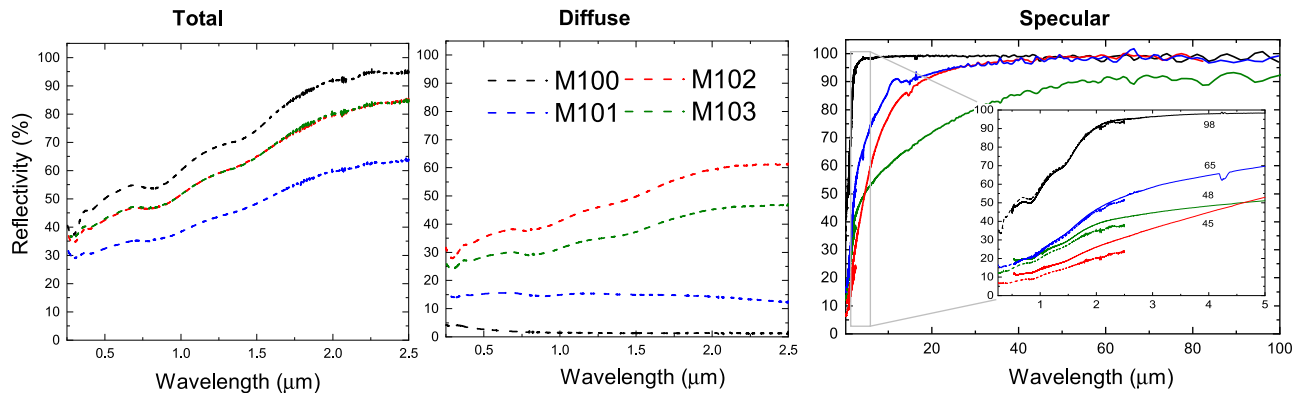
FIG. 5. Total, diffuse, and specular reflectivities measured for the W samples M100-M103. Reflectivity of the W samples measured by the integrating sphere (dashed lines) and FTIR (solid lines). In the inset, both measurements in the range 0.25–5 μm are plotted. Reflectivity values at 4 μm are displayed in the inset.

specular reflectivity measured by an FTIR in the range 0.5–100 μm is displayed. Good agreement between both spectrophotometers is demonstrated. Interestingly, for samples M102 and M103, in the range 0.25–4.6 μm, the specular reflectivity does not follow the corresponding roughness measurements, i.e., a decrease in specular reflectivity for increasing roughness. In fact, it is possible to calculate the specular reflectivity with the well-known Bennett's formula,[13] which correlates the specular reflectivity at normal incidence with the surface roughness,

$$R_s = R_0 \times \exp\left(\frac{-(4 \times \pi \times RMS)}{\lambda^2}\right)^2, \tag{3}$$

where R_s is the resulting specular reflectivity, R_0 is the reflectivity of an ideally smooth surface of the same material, rms is the root mean square roughness, and λ is the wavelength of light. The formula describes a decrease in the reflection as a function of the rms roughness of the surface. At a perfectly smooth surface (rms = 0), the reflectivity equals the square of the Fresnel reflection. Goossens *et al.*,[14] described nearly perfect agreement for smooth samples; for the rougher samples, the deviation between the experiment and the model is larger. Even though the same trend is still visible, Bennett's formula becomes inadequate to predict the specular reflectivity as the surfaces become rougher.

The reflectivity of M102 and M103 follow Bennett's formula only for wavelength values higher than 4.6 μm. As seen in Fig. 4, the scratches on the surface of sample M102 have a width less than 4.6 μm and always contribute to scattering of light below this wavelength. For M103, the surface at high wavelength is affected by large holes (>50 μm), but for a wavelength below 4.6 μm, the surface is less scratched than in M102.

Reflectivity measurements were performed using an ellipsometer at incidence angles of 40°, 60°, 70°, and 75° for s and p polarized lights on the sample M100. s and p reflectivities are plotted for a wavelength of 0.65 μm in Fig. 6. The full line in Fig. 6 represents the s and p components calculated with the theoretical optical constants[15] using the Fresnel equation. The refractive index (n) and extinction coefficient (k) for this film are 2.4 and 2.9, respectively,

at 0.65 μm. In Fig. 6, the value at 0° is the one measured with the spectrophotometer (Cary setup). The measured value with the Cary setup is quite in agreement with the ellipsometer measurement. At 90°, the value is extracted from the calculated curve. This value is equal to 100%, indicating that the material surface is fully specular at a grazing angle.

For all tested surfaces, the BRDFs were measured in the plane of incidence ($\phi_i = \phi_r = 0$), in the orthogonal plane ($\phi_i = 0$ and $\phi_r = 90$), and over the reflection hemisphere (variables θ_i and θ_r). In this way, it is shown that the W sample BRDF is independent of the sample rotation.

The BRDF results for the 4 W surfaces are presented in Fig. 7. The BRDF is plotted vs the detection angle for different incident
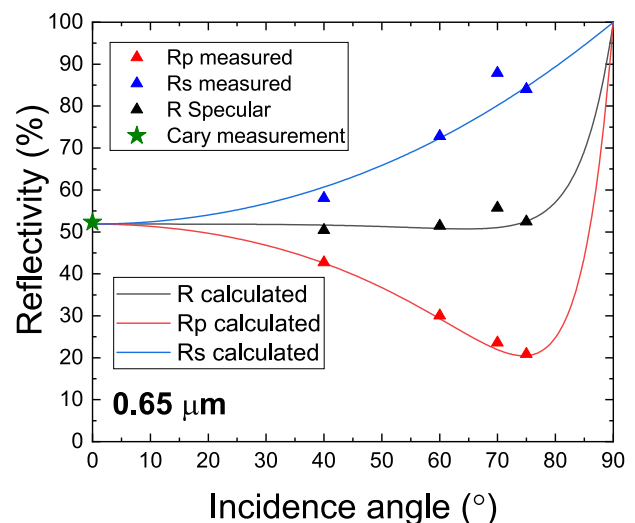

FIG. 6. M100 reflectivities at 40°, 60°, 70°, and 80° for s and p polarizations at 0.65 μm (triangle symbol). The solid lines represent the s and p components fitted from n and k.
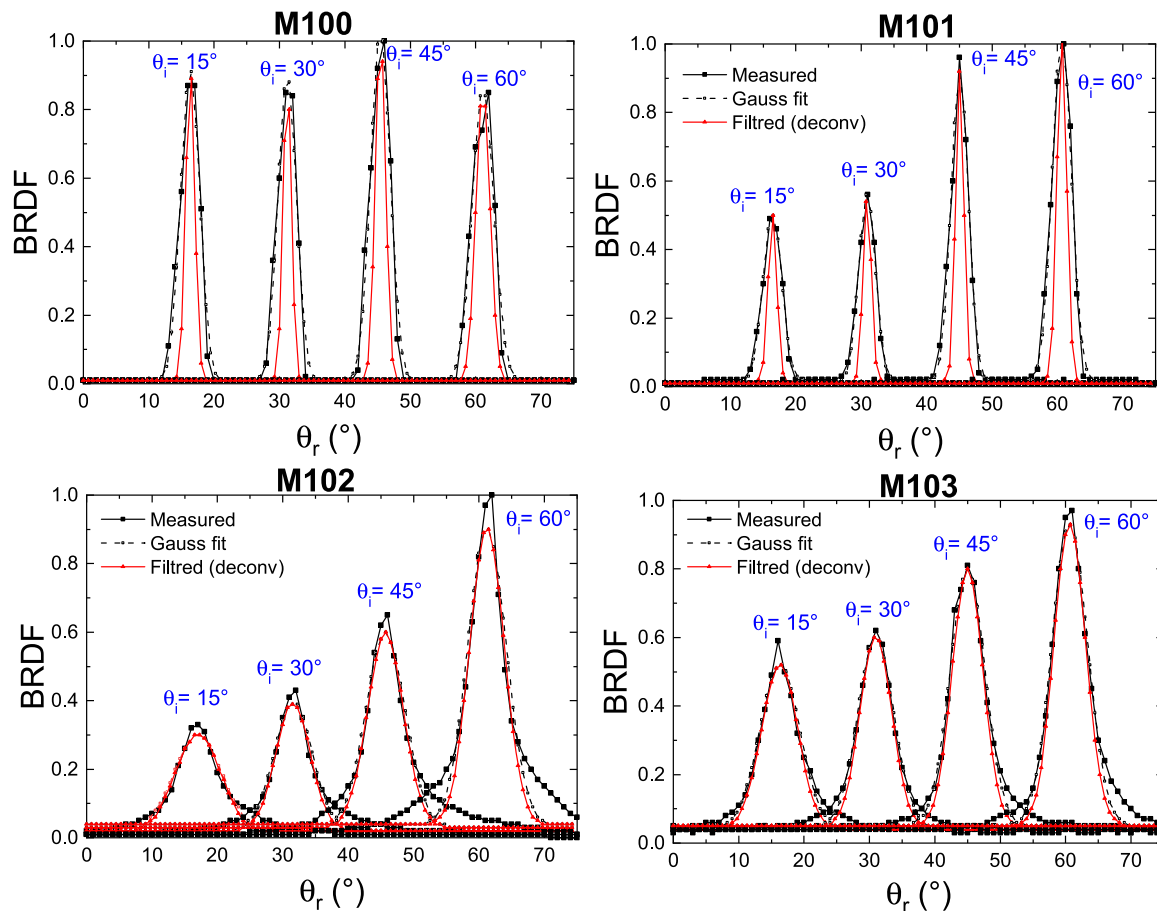
FIG. 7. W sample normalized BRDF results for $\lambda = 0.9\ \mu$m and a variable incident angle.

angles at a fixed wavelength of 0.9 μm. The black line curves represent the measurement results while the red line is for the corrected measurement by subtracting the effect of a non-collimated light source. All results were fitted with a Gauss function centered at the specular direction ($\theta_i = \theta_r$) represented in the figure by a dashed line. No constant reflectance component was measured. This indicates that both samples have only pure Gaussian reflectance around the specular and do not present any Lambertian (or diffuse) component (presented by the inset in Fig. 1). Besides, for all samples, the BRDF increases toward grazing angles.

The Gaussian Full Width at Half Maximum (FWHM) at 15° incidence angle is plotted in Fig. 8 for wavelength values ranging from 0.25 to 1.1 μm. The FWHM stayed almost constant in the entire range, and all values are below 10°. As explained previously for the diffuse and roughness correlation of M102 and M103, the FWHM of the latest is lower than that for M102. For samples M100 and M101, representing the smallest Ra values (0.015 and 0.045 μm, respectively), the FWHM is around 2°. This value is around 4–5 times higher for the rough samples M102 and M103.

Su *et al.*[16] adopted the optical roughness instead of surface roughness in their BRDF model. The optical roughness (σ_{opt}) can

be expressed as the ratio between surface roughness (σ_0) and wavelength (λ),

$$\sigma_{opt} = \frac{\sigma_0}{\lambda}. \tag{4}$$

According to studies by Su *et al.*[16] and Wen and Mudawar,[17] the surface can be classified in three regions with respect to the surface roughness: (i) the specular region when $0 < \sigma_{opt} < 0.2$ for which Bennett's law can be applied to get directional reflectivity, (ii) the intermediate region when $0.2 < \sigma_{opt} < 1$ for which approximate models are needed to describe the BRDF, and (iii) the geometric region when $\sigma_{opt} > 1$ for which the geometric optics law can be used. Su *et al.*[16] presented a plot of the BRDF for five incidence angles and three optical roughness values—0.1, 0.2, and 0.3—for a pure specular surface. As seen in Fig. 7 and reported by Su *et al.*,[16] the maximum of the BRDF value is increasing for an increasing angle, and the FHWM is increasing for higher σ_{opt}. For = 0.9 μm (wavelength at which the BRDF is presented in Fig. 7), the σ_{opt} values are 0.063, 0.2, 0.59, and 1.24 for M100, M101, M102, and M103, respectively.

Theoretical models like those proposed by Torrance and Sparrow[18] assume the reflection of incident radiation to be specular
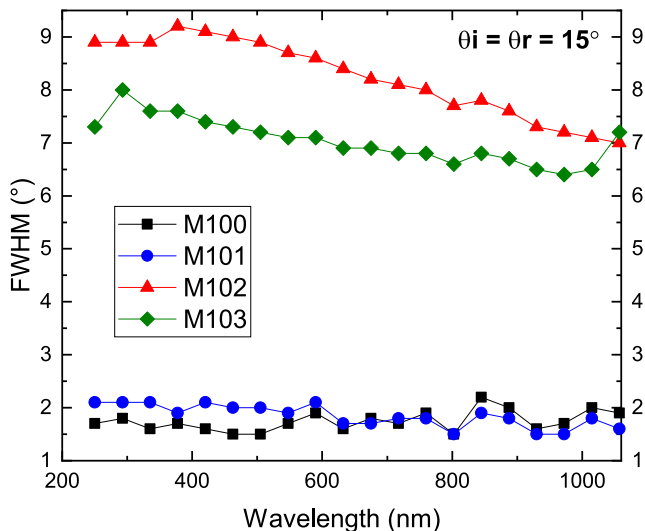
FIG. 8. W sample FWHM variation as a function of the wavelength (data extracted from Fig. 7).

for σ_{opt} below 1 or even below 0.2, such as in the study by Wen and Mudawar.[17] For our samples M100, M101, and M102, σ_{opt} is below 1, and only M100 and M101 have $\sigma_{opt} < 0.2$.

B. Emissivity model

Using Kirchhoff's Law, the spectral normal emissivity of W reference samples is directly calculated from spectral directional hemispherical total reflectance measured by the integrating sphere and FTIR (presented in Fig. 5). Results are shown is Fig. 9. As can be seen, the emissivity increases with roughness for the entire wavelength range. The only exception is for sample M101. That would suggest
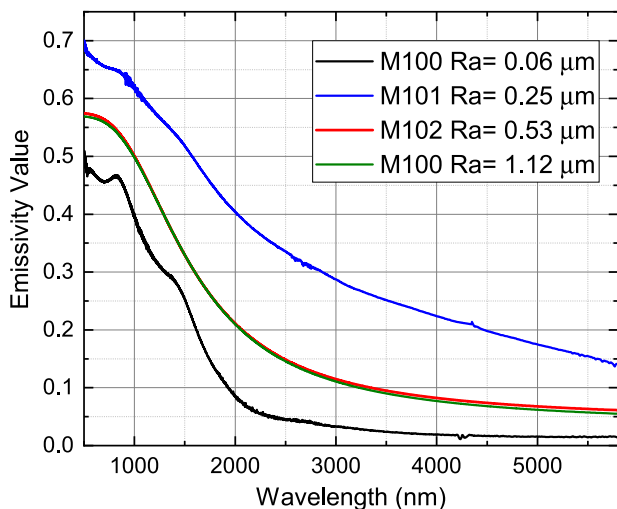
that the average roughness parameter is not able to describe all the complex features on the surface. Other measures of the roughness seem to include other complex features on the surface: high amplitude, low frequency (scratches), and correlation length (machining).[19,20] For all samples, the emissivity decreases with increasing wavelength; in particular, a drop by a factor of 5 from the visible ($\lambda < 0.8$ μm) to the IR range ($\lambda > 2.5$ μm) is measured for M100 samples.

The integration of the BRDF over a hemispherical solid angle gives the spectral hemispherical reflectance at a given incidence angle [$\rho(i)$]. The spectral directional emissivity at a given emission angle [$\varepsilon(e)$] can then be deduced using Kirchhoff's law: $\varepsilon(e) = 1 - \rho(i)$. The emission angular dependence is described with a cosine n power model: n = 1 is for Lambertian distribution; for n > 1, emission will be concentrated around the normal of the surface, and for n < 1, the emission is more evenly distributed across all emission angles with non-negligible contribution of high emission angles (so-called "grazing angles"). The n coefficient results are presented in Fig. 10. For samples M101, M102, and M103, the n coefficient is found to be lower than 1 in the visible range, favoring the grazing angle.

C. Simulation results

The main infrared source in the tokamak comes from the heat flux deposited on the plasma-facing components and in particular on the lower divertor, which is situated at the bottom of the vacuum vessel and receives a maximum heat flux of up to 10 MWm^2 (steady-state) and 20 MW/m^2 (slow transients). The plasma is transparent in the IR range. The WEST thermography system has been designed to operate at 3.9 μm ($\pm$100 nm) to monitor a wide temperature range from 90 to 3400 $^\circ$C (melting temperature of tungsten). In the simulation, only the IR source coming from the divertor is considered (turned on) to assess the reflections coming from these components. Figure 11 compares the experimental image of
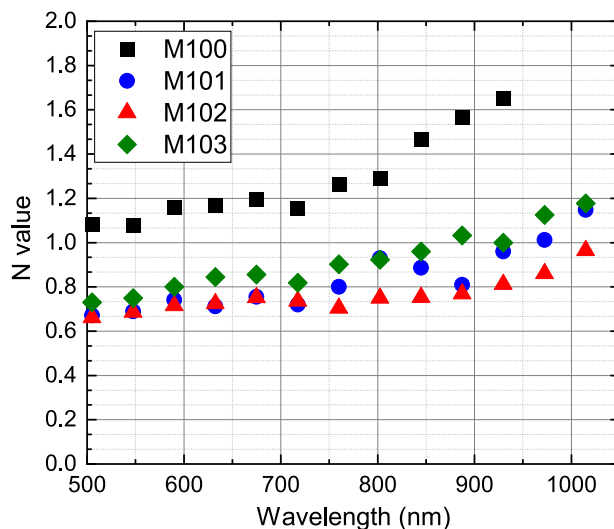

FIG. 9. Spectral normal emissivity as a function of wavelength for M100 to M103 samples.

FIG. 10. W reference sample n factor fitted from the n cosine power model of the directional emissivity.
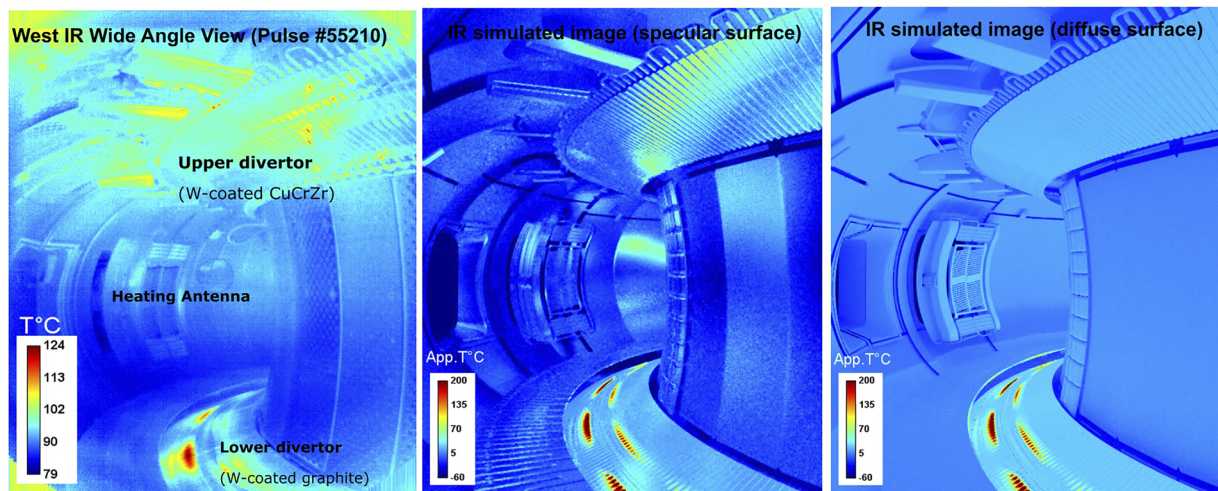
FIG. 11. (Left) Infrared experimental image of WEST wide angle tangential view [3300–3400 nm filter band], (middle) the simulated image assuming a high specular surface further to W sample measurement in the laboratory, and (right) the simulated image assuming all diffuse surfaces.

the WEST wide angle tangential view with the simulated ones by considering two scenarios of a full diffuse surface for in-vessel components (in emission and reflectance) and a high specular surface roughly adjusted to W sample measurements (M103). Table I summarizes the parameters roughly adjusted to laboratory measurement used as input for the photonic simulation. Similar reflection features are observed on experimental and simulated images, especially on the upper divertor, when considering specular reflectance roughly adjusted to experimental data. It is worth noting that other physical phenomena are involved and not completely modeled (as the bubble on the floor), which explains the quantitative difference between the simulated and experimental images. Further analysis of the experimental data shows that the emission model is not (spatially) uniform on the same components during the WEST experimental campaign (depending to erosion/deposition phenomena by plasma). Further simulation should take the emissivity variation into account and check if the associated reflectance model (BRDF) is also affected.

TABLE I. Input parameters for the SPEOS simulation.

WEST components	Materials	Measurement				Parameters used for simulation		
		Ra (μm)	Emissivity @ 4 μm	N power Emissivity	Reflectance model @ 2 μm	Emissivity	N power emissivity	Reflectance
Lower divertor	W-coated graphite	1.8	0.03	...	Specular but with max R shifted	0.1	1	Specular (7°)
		1.1 (M103)	0.09 (M103)	N = 1.5	Highly specular (8°)			Specular (7°)
Baffle	W-coated graphite	...	...		...	0.1	1	Specular (7°)
Inner bumper	W-coated CFC (PVD)	3.2 6.2	0.16 0.09	...	Specular but with max R shifted	0.15	1	Specular (7°)
Outer bumper (LPA)	W-coated CFC (PVD)	3200 nm	0.16	...	...	0.15	1	Specular (7°)
Upper divertor	W-coated CuCrZr	...	...	...	...	0.1	1	Specular (7°)
Heating antenna bumper	W-coated CFC (VPS)	...	...	...	...	0.15	1	Specular (7°)

VI. CONCLUSION

This paper presented an accurate experimental tool available for the optical property measurements of PFC materials, mainly the bidirectional reflectance distribution function. The BULGO was developed for this purpose and showed, after calibration, good accuracy in comparison to another setup (FIGOS). BRDF first results of the W samples with different surface topographies show that their reflectance is represented by a pure Gaussian component around the specular direction with an angular width of less than 10°. The angular dependence of emissivity can be fitted with a cosine n power model. On the other hand, the Gaussian FWHM was found to be almost constant with the wavelength. It is found that roughness has an impact on the BDRF of samples but it does not represent the only factor to describe it.

Experimental data were implemented in the ray-tracing software SPEOS in order to have a better interpretation of the images of the WEST camera and distinguish the patterns caused by the reflection of the W divertor. By comparing simulated and experimental images in WEST, the experimental results were confirmed, including the Gaussian response and the angular dependence of reflectance of the W divertor material.

ACKNOWLEDGMENTS

DATA AVAILABILITY

The data that support the findings of this study are available from the corresponding author upon reasonable request.

REFERENCES

[1] M.-H. Aumeunier, M. Firdaouss, J.-M. Travère, T. Loarer, E. Gauthier, V. Martin, D. Chabaud, E. Humbert, and JET-EFDA Contributors, "Modeling of the ITER-like wide-angle infrared thermography view of JET," Rev. Sci. Instrum. **83**, 10D522 (2012).

[2] M.-H. Aumeunier, Y. Corre, M. Firdaouss, E. Gauthier, T. Loarer, J. M. Travère, and J. L. Gardarein, "Multi parametric sensitivity study applied to temperature measurement of metallic plasma facing components in fusion devices," in *2013 3rd International Conference on Advancements in Nuclear Instrumentation, Measurement Methods and their Applications (ANIMMA)* (IEEE, 2013), pp. 1–6.

[3] T. Loarer, "Surface temperature measurement of plasma facing components in metallic environment," Contrib. Plasma Phys. **51**, 201–206 (2011).

[4] S. Amiel, T. Loarer, C. Pocheau, H. Roche, M. H. Aumeunier, E. Gauthier, C. L. Niliot, and F. Rigollet, "Surface temperature measurement of plasma facing components with active pyrometry," J. Phys.: Conf. Ser. **395**, 012074 (2012).

[5] M. Kočan, R. Reichle, M.-H. Aumeunier, J. P. Gunn, S. Kajita, F. Le Guern, S. W. Lisgo, T. Loarer, A. S. Kukushkin, A. S. Naik *et al.*, "First results on modeling of ITER infrared images," Phys. Scr. **2016**, 014047.

[6] M.-H. Aumeunier, M. Kočan, R. Reichle, and E. Gauthier, "Impact of reflections on the divertor and first wall temperature measurements from the ITER infrared imaging system," Nucl. Mater. Energy **12**, 1265–1269 (2017).

[7] S. Kajita, M.-H. Aumeunier, E. Yatsuka, A. Alekseev, E. Andreenko, A. Kukushkin, V. Neverov, M. Kocan, M. Bassan, E. Veshchev *et al.*, "Effect of wall light reflection in ITER diagnostics," Nucl. Fusion **57**, 116061 (2017).

[8] See https://www.ansys.com/products/optical/ansys-speos for information.

[9] J. F. Murray-Coleman and A. M. Smith, "The automated measurement of BRDFs and their application to luminaire modeling," J. Illum. Eng. Soc. **19**, 87–99 (1990).

[10] K.-D. Zastrow, S. R. Keatings, L. Marot, M. G. O'Mullane, G. de Temmerman, and JET-EFDA Contributors, "Modeling the effect of reflection from metallic walls on spectroscopic measurements," Rev. Sci. Instrum. **79**, 10F527 (2008).

[11] J. Schopfer, S. Dangel, M. Kneubühler, and K. Itten, "The improved dual view field goniometer system FIGOS," Sensors **8**, 5120–5140 (2008).

[12] B. Eren, L. Marot, M. Wisse, D. Mathys, M. Joanny, J.-M. Travère, R. Steiner, and E. Meyer, "*In situ* evaluation of the reflectivity of molybdenum and rhodium coatings in an ITER-like mixed environment," J. Nucl. Mater. **438**, S852–S855 (2013).

[13] H. E. Bennett, M. Silver, and E. J. Ashley, "Infrared reflectance of aluminum evaporated in ultra-high vacuum," J. Opt. Soc. Am. **53**, 1089–1095 (1963).

[14] V. Goossens, N. Gotzen, S. Van Gils, E. Stijns, G. Van Assche, R. Finsy, and H. Terryn, "Predicting reflections of thin coatings," Surf. Coat. Technol. **204**, 551–557 (2009).

[15] E. D. Palik, *Handbook of Optical Constants of Solids* (Academic Press, 1998), Vol. 3.

[16] P. Su, Q. Eri, and Q. Wang, "Optical roughness BRDF model for reverse Monte Carlo simulation of real material thermal radiation transfer," Appl. Opt. **53**, 2324–2330 (2014).

[17] C.-D. Wen and I. Mudawar, "Modeling the effects of surface roughness on the emissivity of aluminum alloys," Int. J. Heat Mass Transfer **49**, 4279–4289 (2006).

[18] K. E. Torrance and E. M. Sparrow, "Theory for off-specular reflection from roughened surfaces," J. Opt. Soc. Am. **57**, 1105–1114 (1967).

[19] E. S. Gadelmawla, M. M. Koura, T. M. A. Maksoud, I. M. Elewa, and H. H. Soliman, "Roughness parameters," J. Mater. Process. Technol. **123**, 133–145 (2002).

[20] M.-H. Aumeunier, J. Gerardin, C. Talatizi, M. Le Bohec, M. Ben Yaala, L. Marot, T. Loarer, R. Mitteau, J. Gaspar, F. Rigollet *et al.*, "Infrared thermography in metallic environments of WEST and ASDEX Upgrade," Nucl. Mater. Energy **26**, 100879 (2021).